Shake table test of a masonry building retrofitted with shotcrete

Amirhossein Ghezelbash[1], Katrin Beyer[2], Kiarash M. Dolatshahi[1*], and Mohammad Yekrangnia[3]

[1]Department of Civil Engineering, Sharif University of Technology, Tehran, Iran

[2]Department of Civil Engineering, Ecole Polytechnique Fédérale de Lausanne (EPFL), Lausanne, Switzerland

[3]The Organization for Development, Renovation and Equipping Schools of Iran (DRES), Tehran, Iran

Abstract

This paper presents the results of a series of shake table tests carried out on a half-scale single-story unreinforced masonry building with asymmetric openings. First, the unretrofitted building is subjected to seven increasing steps of bidirectional seismic excitation. The damaged building is then rehabilitated using steel mesh and shotcrete layer with two walls retrofitted from the exterior face and the other two from the interior face. Afterward, the shake table test is again conducted on the retrofitted specimen in nine increasing excitation levels. Three cases of interior-to-interior, interior-to-exterior, and exterior-to-exterior shotcrete connections are considered at the intersection of perpendicular walls, and for each case, the development of cracks is investigated. Moreover, the effects of fixity of the shotcrete vertical rebars in the foundation are investigated through releasing the rebar-foundation connection in the last three steps of the test on the rehabilitated specimen. The results indicate the adequacy of the retrofit method in creating a strong bond that leads to an acceptable composite action between the brick layer and shotcrete; though, concentrated cracks were observed at the connections of the perpendicular walls. Furthermore, the shotcrete layer has proven to be able to prevent further propagation of the previously developed cracks, which can provide a practical solution for rehabilitation of damaged masonry buildings.

Keywords

Shake table test; URM buildings; Seismic retrofit; Shotcrete; Damaged buildings rehabilitation

1. Introduction

In Iran, despite the poor seismic performance of unreinforced masonry (URM), many school buildings are constructed as unreinforced masonry (URM) buildings. In 2003, the Bam earthquake in southeastern Iran caused 26,000 casualties and over 30,000 injuries because of the collapse of thousands of adobe and URM buildings [1]. As a result, a national program was put in place to assess the seismic safety and performance of school buildings in Iran [2]. The program focuses especially on URM buildings, which constitute the majority of school buildings throughout Iran. Moreover, the focus has been put on mitigating seismic risk through a large-scale retrofit program. Since 2005, over three billion US dollars has been spent on school retrofit in Iran by the Organization for Development, Renovation and Equipping Schools of Iran (DRES) as the only organization responsible for construction and maintenance of schools throughout Iran. As a result, a significant amount of development work has been conducted to evaluate various assessment methodologies and evaluate possible retrofit methods [3].

There are various retrofit techniques for upgrading masonry buildings; all of which aim at improving one or several response characteristics, i.e., effective stiffness, ultimate strength, ductility, and energy dissipation capacity. Following is a brief review of some of the available retrofit techniques for URM buildings. Reinforcing masonry walls with mesh grids has proved a good retrofit technique during past earthquakes and by many shake table tests, as well. Several of these shake table tests proved the effectiveness of the polymer grids in improving the integrity and homogeneity of the masonry structure [4–6]. The main drawback on using polymer mesh as a retrofit solution for masonry buildings is its hyper-elastic behavior, which requires significant deformations to be activated in the load-bearing mechanism [7]. Apart from their costs, they are vulnerable to Ultraviolet (UV) radiation from the sun if not embedded in a mortar matrix [8]. On the other hand, steel welded mesh has become adopted by some regions to be widely used as the main retrofit elements with satisfactory improvement in the seismic performance of URM buildings [9,10]. Using vertical and horizontal rubber or steel strips and straps on masonry walls in order to tie the discrete masonry blocks together, can be regarded as another solution for seismic rehabilitation of these structures [11]. Drilling holes over the entire height of the wall and inserting reinforcement bars at subsequent distances and then filling the holes with grout significantly increases shear and flexural capacity of URM walls [12]. The walls can be reinforced by tying the vertical retrofitting components to the walls by nylon threads. The rods can be in the form of steel bars, cane, or bamboo [13]. In the case of using horizontal and vertical straps on the wall's surface, these elements can be prestressed in order to increase walls' tensile and shear resistance.

* Corresponding author, Email: dolatshahi@sharif.edu, Tel: +98-21-6616-4219

One of the effective solutions to improve the seismic behavior of URM buildings is shotcreting the walls' surface. Regardless of the employed methods which can be dry-mix or wet-mix, mortar or concrete is conveyed through a hose and is projected at high velocity on walls' surface. Usually, at least a layer of reinforcing bars grid is placed on the walls' surface to improve tensile and shear capacity of shotcrete. The thickness of the shotcrete and the reinforcing grid can be adapted to the seismic demand. In order to transfer the shear stress across the shotcrete-masonry interface, shear dowels are fixed using epoxy or cement grout into holes drilled into the masonry wall [14]. Abrams et al. [15] studied the effectiveness of four retrofit methods through static cyclic tests on a masonry pier. The methods included adhered fiber-reinforced polymer strips, reinforced shotcrete overlay, ferrocement surface coating, and grouted reinforcing bars within drilled cores. The concrete layer of the shotcreted specimen experienced cracks at its base in 0.2% lateral drift ratio, and the cracks propagated to the masonry face at 0.3% drift ratio. During the next cycles, the wall rocked about the base crack, elongating the vertical reinforcement into the plastic range. When the cycles were reversed, the vertical reinforcement did not compress to its original length, causing the wall to lean away from the shotcrete surface. The maximum drift was 1.5% at which point the wall was tilting out-of-plane, and the masonry started to crush. They reported that the specimens retrofitted by shotcrete showed the highest initial stiffness, yield strength, and dissipated energy among all other specimens. The same results were acquired by Lin et al. [16] who conducted diagonal compression tests on 25 clay brick URM wallettes to investigate the increase in shear strength for a range of shotcrete thicknesses applied to the masonry wallettes as externally bonded shotcrete reinforcement. They reported that the effectiveness of the retrofit method remained constant for one and two leaf wallettes, but decreased rapidly for wall thicknesses greater than two leaves. The ductility of the strengthened specimens showed an average increase of 3.2 times that of the reference specimens. A comparable increase in strength capacity of 3.6 times was observed by ElGawady et al. [17] who carried out static cyclic tests on hollow clay block URM walls shotcreted by a reinforced overlay. The possible benefit of using anchors for connecting the shotcrete reinforcement layer to the Reinforced Concrete (RC) foundation was studied by Shabdin et al. [18] by performing static cyclic rests on five full-scale specimens with two different height-to-length aspect ratios. Two specimens were tested as reference, and others were strengthened on a single face using shotcrete layer. The failure mode in both reference and strengthened slender walls was rocking. The shotcrete layer contributed to improving the stiffness, strength, and energy dissipation, because of yielding and rupture of steel bars anchored to the foundation. On the other hand, in strengthened squat walls, shotcrete layer increased the shear sliding capacity with marginal improvement in rocking capacity. Consequently, the failure mode of strengthened walls changed from shear sliding to rocking, even in the specimen with anchorage. Though, anchorage system was able to improve the out-of-plane performance of strengthened walls. Ghiassi et al. [19] proposed analytical-based relations for design and seismic evaluation of shotcreted URM walls. They considered four failure modes for these walls, namely flexural, diagonal tension, shear sliding, and compressive behaviors. The strength relations and acceptance criteria for each of them are provided in accordance with FEMA 356 [20] and ASCE 41 [21] relations for reinforced concrete and masonry walls. The accuracy of the proposed relations in predicting the force-displacement behavior and governing failure modes of these walls is validated by comparing the results with available experimental results.

Although much has been achieved in reducing the structural damages to as minimum as possible thanks to shotcreting of thousands of URM school buildings in Iran [22], there are still ambiguities regarding the efficiency of some details of the retrofit methods and also regarding the possibility of optimizing some of the details such as wall-to-roof, wall-to-wall, and wall-to-foundation connections. In response to this need, this study aims at understanding the effectiveness of some of the available details that can be used interchangeably in terms of connection of shotcrete to the foundation and the connection of perpendicular walls. This paper summarizes the results of a shake table test series on a typical Iranian URM school building, which was first tested in unretrofitted and then in retrofitted configuration. The tests were carried out at the Earthquake Engineering Research Center (EERC) of Sharif University of Technology (SUT) and were jointly supported by Ecole Polytechnique Fédérale de Lausanne (EPFL), Switzerland, and Sharif University of Technology along with the technical advice from experts in DRES. The test setup and specimen characteristics are presented first, along with a summary of construction and retrofit procedures. The instrumentation and input ground motion are described afterward. A summary of the excitation sequence is then given, followed by the results of both tests, presented together in detail.

2. Outline and objectives

The failure modes observed in URM buildings are generally categorized to (1) in-plane diagonal and horizontal cracks of load-bearing and non-bearing walls, (2) out-of-plane overturning of load-bearing and especially non-bearing walls, (3) rocking of the piers adjacent to openings, (4) toe crushing or crack propagation at the corner of the walls and openings, and (5) sliding of the floor slabs on the walls. Figure 1 shows the failure modes observed in masonry buildings during the November 2017 Kermanshah earthquake in Iran. The most common failure was diagonal shear

cracks of walls, shown in Figure 1(a). In many cases, the walls openings had influenced the crack pattern of the perpendicular walls. For example, in Figure 1(b), the crack of the wall was developed from the point which corresponds to the corner of the window in the perpendicular wall. In a few cases, such as the one in Figure 1(c), separation of perpendicular walls was observed at the corner of the buildings. Moreover, some cases exhibited sliding between the roof and the internal walls, as shown in Figure 1(d), due to improper roof-to-wall connection detailing.

(a) Diagonal crack of walls (b) Concentrated cracks (c) Separation of walls (d) Sliding of the roof

Figure 1. Failure modes observed in previous earthquakes [23]

If applied correctly, each retrofitting method is aimed to reduce the occurrence probability of one or several failures in a given seismic demand and to improve the integrity and flexibility of the structure. To develop an economically viable and well-validated retrofit method for masonry school buildings, a half-scale model of a typical room of a school building was constructed and tested on the shake table facility at Sharif University of Technology. First, the unretrofitted specimen (URM) was constructed, and a series of bidirectional shake table tests were applied up to a damage level which allowed investigating the failure modes, evaluating the behavior of the unretrofitted specimen, and highlighting the weak points of the specimen without reaching collapse. The geometry considered for the specimen allowed for different failure modes to take place in different regions of the specimen, such as the crack propagation between perpendicular walls, and the in- and out-of-plane cracks on the walls. Then, the damaged specimen was repaired using steel mesh and shotcrete layer, and another series of shake table tests were conducted to excite the retrofitted specimen (RM) up to near the collapse point. At each excitation level, an investigation was made on the effects of the retrofitting details at each part of the specimen, such as the connection between the roof and the walls, the connection between the shotcretes of the perpendicular walls, the connection considered for the vertical rebars of the shotcrete at the foundation level. Furthermore, the composite action between the shotcrete layer and the walls was studied by comparing the crack patterns of the interior and exterior faces of each wall. At last, the response of the specimen, before and after retrofit was compared to quantify the overall response improvements, i.e., stiffness, strength, and ductility increase, caused by the retrofit strategy.

3. Experimental program

This section describes the fabrication procedure of the URM specimen. Since a half-scale model was used, first the similitude law and all dimensions are described in detail. The design of wall-to-roof, wall-to-wall, and wall-to-foundation connections of the RM specimen are then discussed as follows. Material properties, instrumentation, and input ground motion are also covered in this section.

3.1 Similitude law

The specimen was built with a 1:2 scale factor considering the size and capacity of the shake table. Previous studies [24] recommended employing Cauchy and Froude similitude laws [25] to achieve nonlinear behavior as close to the prototype behavior as possible. The scale factor of each parameter is calculated using Cauchy, and Cauchy and Froude similitude laws, presented in Table 1. Cauchy and Froude similitude laws maintain the acceleration equal to the real ground motion and require a scale factor of four for the mass of the model, which cannot be achieved unless the model is built with new materials that have a specific mass two times of that of the original material. Alternatively, most of the previous studies [24,26,27] have used the same materials for the models with an artificial mass added to the floors of the model to satisfy the mass scale factor. In this study, the 1:2 scale of the specimen required using an artificial mass equal to the mass of the model, which was not achievable because of the capacity of the shake table; thus, it was decided to use Cauchy similitude law instead. Cauchy similitude law allows a scale factor of eight for the mass and in return, amplifies the prototype ground motion acceleration by a scale factor of two. Note that while the horizontal accelerations are scaled in this study, due to the absence of the vertical degree of freedom in the shake table, the effect of the similitude law on gravitational acceleration is neglected, i.e., the axial stresses due to gravity in the model are only half the corresponding stresses in the prototype. Hence, a full-scale prototype is expected to show higher in- and out-of-plane strength, with lower in-plane rocking and out-of-plane mechanisms at the piers adjacent to the openings,

and at the building corners [28]. Nevertheless, the actual axial load effect requires further investigation via numerical models. Moreover, for the RM test, an additional mass was added to the roof of the specimen. The extra mass was not a part of similitude law and only was considered in order to increase the intensity of the shake table excitation.

Table 1. Similarity scale factors for a 1:2 scale dynamic model

Parameter	Symbol	Model-to-Prototype conversion scale factors		
		General equation	Cauchy and Froude laws	Cauchy law
Length	L	$\lambda_L = L_p / L_m = \lambda$	$\lambda_L = \lambda = 2$	$\lambda_L = \lambda = 2$
Young's modulus	E	$\lambda_E = E_p / E_m$	$\lambda_E = 1$	$\lambda_E = 1$
Specific mass		$\lambda_\rho = \rho_p / \rho_m$	$\lambda_\rho = \lambda^{-1} = 0.5$	$\lambda_\rho = 1$
Area	A	$\lambda_A = A_p / A_m$	$\lambda_A = \lambda^2 = 4$	$\lambda_A = \lambda^2 = 4$
Volume	V	$\lambda_V = V_p / V_m$	$\lambda_V = \lambda^3 = 8$	$\lambda_V = \lambda^3 = 8$
Mass	m	$\lambda_m = m_p / m_m$	$\lambda_m = \lambda^2 = 4$	$\lambda_m = \lambda^3 = 8$
Displacement	d	$\lambda_d = d_p / d_m$	$\lambda_d = \lambda = 2$	$\lambda_d = \lambda = 2$
Velocity	v	$\lambda_v = v_p / v_m$	$\lambda_v = \lambda^{0.5} = \sqrt{2}$	$\lambda_v = 1$
Horizontal acceleration	a	$\lambda_a = a_p / a_m$	$\lambda_a = 1$	$\lambda_a = \lambda^{-1} = 0.5$
Weight	W	$\lambda_W = W_p / W_m$	$\lambda_W = \lambda^2 = 4$	$\lambda_W = \lambda^3 = 8$
Shear force	F	$\lambda_F = F_p / F_m$	$\lambda_F = \lambda^2 = 4$	$\lambda_F = \lambda^2 = 4$
Overturning moment	M	$\lambda_M = M_p / M_m$	$\lambda_M = \lambda^3 = 8$	$\lambda_M = \lambda^3 = 8$
Shear stress in walls		$\lambda_\sigma = \sigma_p / \sigma_m$	$\lambda_\sigma = 1$	$\lambda_\sigma = 1$
Shear strain in walls		$\lambda_\varepsilon = \varepsilon_p / \varepsilon_m$	$\lambda_\varepsilon = 1$	$\lambda_\varepsilon = 1$
Time	t	$\lambda_t = t_p / t_m$	$\lambda_t = \lambda^{0.5} = \sqrt{2}$	$\lambda_t = \lambda = 2$
Frequency	f	$\lambda_f = f_p / f_m$	$\lambda_f = \lambda^{-0.5} = 1/\sqrt{2}$	$\lambda_f = \lambda^{-1} = 0.5$

3.2 Specimen design

The geometry of the specimen is presented in Figure 2. The size of the specimen followed the capacity and size of the shake table, and the layout of the openings followed Iranian regulations [29] to present a common-built 7.4×7.4×4.0 m classroom. The principal west-east (left-right) and north-south (up-down) directions of the floor plan are shown in Figure 2(a) with "L" (Longitudinal) and "T" (Transverse), respectively, and the arrows indicate the positive direction of the shake table actuators. For lintel beams and roof beams, IPE180 profiles [30] were used.

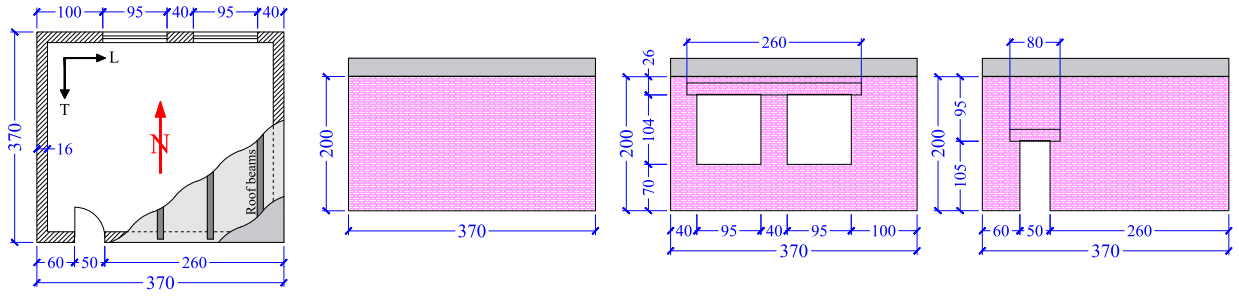

(a) Floor plan (b) East and west walls (c) North wall (d) South wall

Figure 2. Geometry of the specimen (dimensions are in cm)

In the specimen, the typical jack-arch roof was replaced with composite reinforced concrete and steel beam. The roof beams were just seated on the north and south walls in a 10 cm contact length, and were connected to the concrete slab using UNP60 profiles [30] with 20 cm spacing. The composite roof ensured the rigidity of the diaphragm and stiffness-proportional load distribution between the walls. The stiff details of the roof also minimized the chance of collapse and, therefore, allowed focusing on the connections, and in- and out-of-plane behavior of the walls. Half-

scaled clay bricks with the dimension of 10.5×5.0×2.9 cm and 1:1:3 (cement: lime: sand) mortar with 0.5 cm thickness were used in the specimen. The walls were 16 cm thick, constructed with a one-and-a-half brick layout in thickness. In Figure 2, the lintel beams and the tie-beams are shown with hollow rectangles above the openings and filled rectangles on top of each wall, respectively. The lintel beam above the two windows of the south wall was considered continuous to prevent the collapse of the roof in the case of severe damage in the middle pier. Each lintel beam was extended 15 cm from the inner face of the openings; the 15 cm distance was calculated by applying the 1:2 length scale factor to the actual 30 cm spacing recommended by Iranian regulations [31].

In the first phase, the URM specimen was built with different roof-to-wall connection details. The cross-section views of the unretrofitted east and west walls are shown in Figure 3(i). Rebars with 8 mm diameter were used in every part of the specimen. A roof diaphragm of 10 cm thickness was considered to represent the jack-arch roof common in masonry buildings, and to compensate for the removed jack-arch roof materials. The north-to-south direction of the roof beams followed as-built details of masonry buildings; hence, the roof acted as a one-way diaphragm and transferred the roof weight to the north and south walls. The spacing of the embedded steel grid of the roof was designed to be 20 cm based on the allowable rebar spacing of 40 cm. The horizontal tie-beams on top of the walls were designed as a part of the roof-to-wall and roof-to-shotcrete connection, and provided the roof beams with space to sit on the walls. To transfer shear loads between the roof and the walls and to prevent the roof from sliding on the walls, following design was proposed and used in accordance with the technical details from DRES [32]: a set of holes with 30 cm depth were drilled at the middle of the walls thickness, and a 90-degree hooked rebar was inserted in each hole. The holes were filled with grout, and the other ends of the hooked rebars were spliced to the roof steel grid in a 50 cm length.

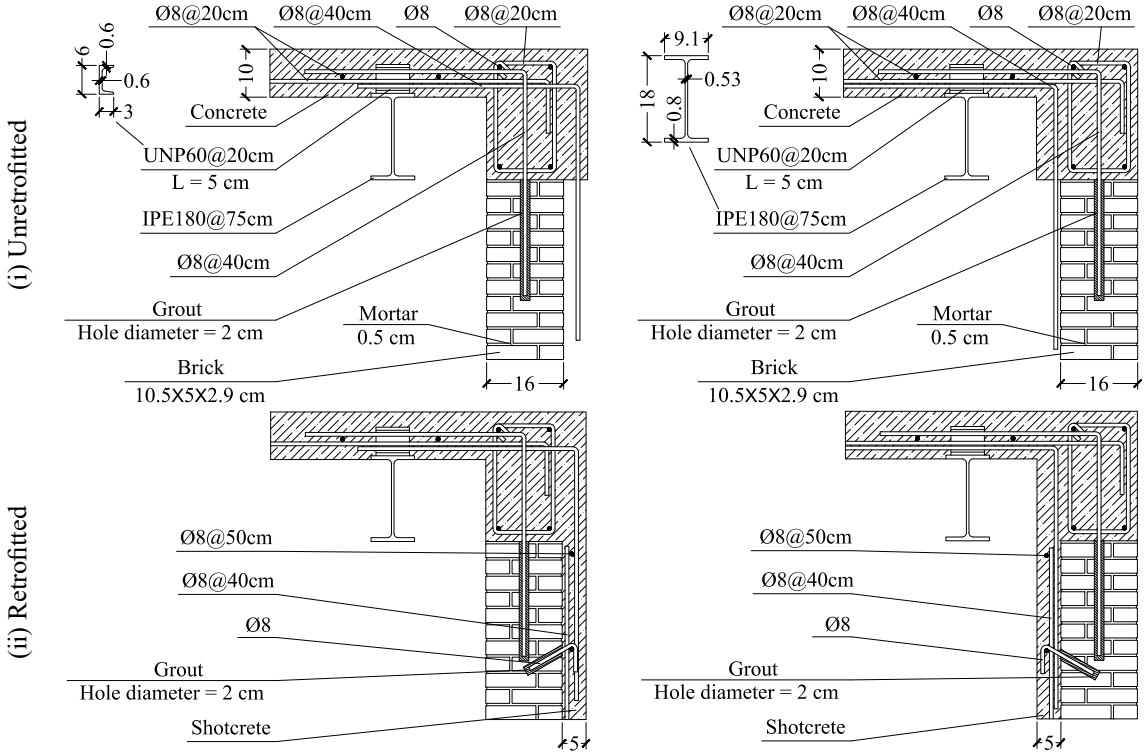

(a) East wall cross-section (b) West wall cross-section

Figure 3. Roof-to-wall connection details: (i) unretrofitted, and (ii) retrofitted configuration (dimensions are in cm)

In the second phase, after the URM test, shotcrete layer was added to the interior faces of the east and the north walls, and exterior face of the west and south walls. Figure 3(ii) shows the cross-section view of the retrofitted east and west walls. During the construction of the URM specimen, a group of 90-degree hooked rebars were placed between the roof reinforcement and the shotcrete face of each wall with 50 cm splice length at each end, to connect the shotcrete reinforcement to the roof. Typical retrofitting details use 10 cm thickness for the shotcrete layer [32], which led to 5 cm thickness for the scaled RM specimen. The vertical and the horizontal rebars were used in 40 cm and 50 cm spacings, respectively, instead of the common 20 cm spacing [32]. While the 0.3% vertical reinforcement ratio satisfies the minimum reinforcement limits of ACI 318 [33], the 0.2% reinforcement ratio does not meet the requirement.

Nevertheless, the numerical studies before the constructions showed a rocking failure for the walls of the RM specimen, where only the vertical rebars would react to the excitation. The 40 cm spacing of the vertical rebars was also designed to ensure that the specimen would undergo reasonable damage before reaching the shake table capacity. A set of 135-degree hooked rebars, shown in Figure 3(ii-a) and Figure 3(ii-b), were placed at all horizontal-vertical rebar intersections to attach the shotcrete layer to the brick walls and to ensure composite action.

The specific layout of the retrofitted specimen resulted in three different shotcrete connection cases at the corners, shown in Figure 4. The plan view for the northeast corner is shown in Figure 4(a) where both perpendicular walls were retrofitted from the exterior face, and the horizontal rebars of the shotcretes were connected by a 90-degree hooked rebar with 50 cm splice length at each end. Similarly, as` shown in Figure 4(b), at the southwest corner of the specimen with both walls having interior shotcrete, a 90-degree hooked rebar with a 50 cm splice length was used. The connection between the shotcrete layers at the northwest and southeast corners, shown in Figure 4(c) was made by drilling a series of holes through the thickness of the wall and passing the 90-degree hooked rebars through the holes. The rebars were spliced to ends of the horizontal rebars in a 50 cm length, and the holes were filled with grout.

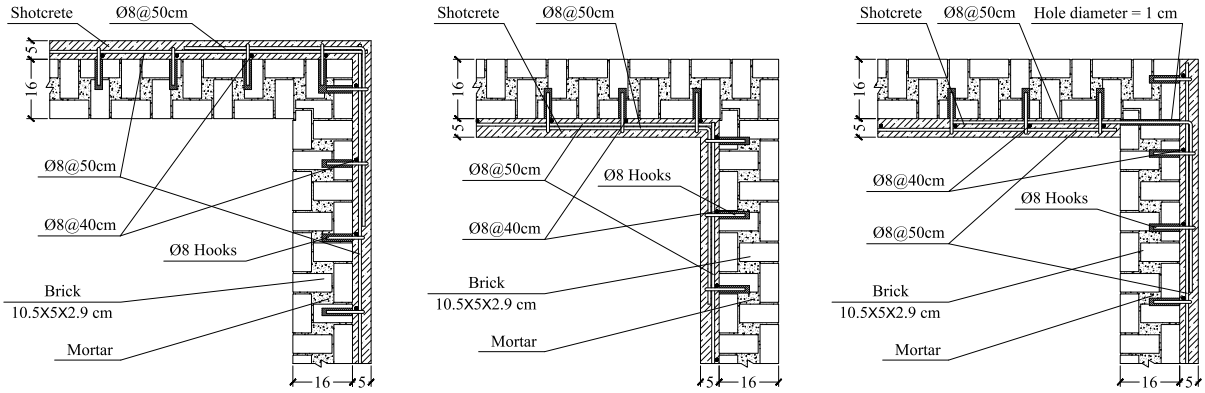

Exterior-to-exterior (northeast cor.) Interior-to-interior (southwest cor.) Exterior-to-interior (other corners)

(a) (b) (c)

Figure 4. Plan view of wall-to-wall connections (dimensions are in cm)

Before the construction process, a steel foundation was placed on the shake table, as shown in Figure 5(a). The connection between the shotcrete layer and the foundation of the retrofitted buildings is commonly made by extending the vertical rebars to the foundation in a 20 cm height [32], which has proved to eliminate the rocking movement and postpone the strength degradation [18]. In this study, the continuity of the vertical rebars in the foundation was simulated by adding custom-sized angle profiles [30] to the steel foundation at the position of each vertical rebar. Each angle profile was connected to the foundation using two M8 bolts, from the side that corresponded to the shotcrete face of the walls. A 60 cm vertical rebar was bolted to each angle profile before the construction process, and later, during the application of the shotcrete layer, each shotcrete vertical rebar was spliced to the pre-installed rebars in a 50 cm splice length. Figure 5(a) presents a view of the described shotcrete-to-foundation connection. The bolted connection allowed comparing the behavior of the specimen with and without connecting the vertical bar to the foundation; as all bolts were removed, and the connections were released during the last three steps of the RM tests.

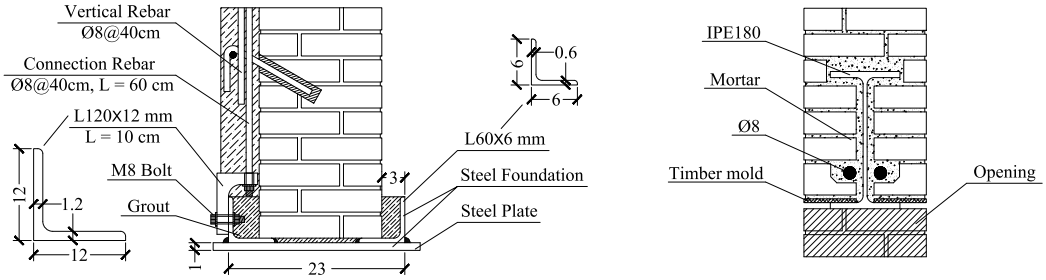

(a) Foundation (b) Lintel beam

Figure 5. Steel foundation and lintel beam details (dimensions are in cm)

The details of the lintel beams are shown in Figure 5(b). For the first row in the height of lintel beams, the bricks were cut in a curved shape and laid on thickness to make room for mortar. A 8 mm rebar was placed at each side of the beams to level the surface for the next brick row. Stronger-than-usual [31] lintel beams were used to prevent the collapse of the roof in case of failure of the piers. As the prototype building would have higher axial stress on the walls, the piers of the prototype would show lower flexural movement, and therefore a weaker lintel beam would suffice for holding the prototype walls.

3.3 Material properties

Table 2 presents the mechanical properties of the material samples collected throughout different periods of construction and retrofitting phases. The tensile rebar strength test was carried out for five 15 cm samples of the shotcrete rebars. The mortar was tested for compressive strength by taking six 10 cm cube samples from different layers of the walls at different ages ranging from 35 to 53 days. Five 16×21×32 cm prism samples were made with eight brick rows in height to investigate the compressive strength of the masonry. The cohesion and friction of mortar joints were determined from direct shear tests of ten 5×10 cm samples built by attaching two bricks, with a layer of mortar in between. Five 15 cm cubic samples were made from the concrete of the shotcrete layer and were tested for compressive strength in the day of the RM specimen shake table test. All samples were cured similar to the specimen. While the 1:1:3 mixture ratio resulted in high mortar cohesive strength (0.27 MPa), the bricks lowered the compressive strength of the masonry prism (2.51 MPa). Nevertheless, both cohesion and compressive strength values are aligned with the properties of the materials used in local constructions [34]. The conjugation of strong mortar and weak bricks is also not in conflict with typical details, and represents a critical state where the cracks can propagate to the bricks.

Table 2. Material component test results

Component	Parameter	Symbol	Unit	Reference	Test results	
					Mean	CoV [%]
Rebar	Yield strength	f_y	MPa	ASTM A370 [35]	368.9	2.3
	Ultimate strength	f_u	MPa	ASTM A370 [35]	559.1	0.3
Mortar	Compressive strength	f_m	MPa	ASTM C109 [36]	23.3	31.1
	Cohesion	c	MPa	Atkinson et al. [37]	0.27	24.8
	Friction coefficient	$\tan\phi$	—	Atkinson et al. [37]	0.82	15.1
	Specific mass	ρ_m	ton/m^3	BS EN 1015-10 [38]	2.1	—
Masonry prism	Compressive strength	f'_m	MPa	ASTM C1314 [39]	2.5	31.0
Brick	Specific mass	ρ_b	ton/m^3	BS EN 772-21 [40]	1.7	—
Shotcrete	Compressive strength	f'_c	MPa	ASTM C39 [41]	7.9	8.2

With 18.0 kN/m^3 as the specific weight of the masonry walls, the geometry and the construction details of the specimen resulted in a total of 74.9 kN weight for the walls, and 56.5 kN for the roof. Therefore, the total weight of the URM specimen was 131.4 kN. In the second phase of the tests, the total weight of the specimen was increased to 164.6 kN by adding 33.2 kN shotcrete to the walls. In addition, four 16 kN steel blocks were added to the roof as additional mass to increase the induced load to the specimen, resulting in a total 228.6 kN weight for the RM specimen.

3.4 Specimen fabrication

Summary of the construction process is shown in Figure 6, highlighting the primary steps in chronological order. The four-part steel foundation was connected to the shake table using four M20 bolts for each part, and the foundation connection angles were installed. The wall-to-foundation connection rebars were bolted to the steel angles before adding the second brick row. The mortar and masonry samples were collected during the construction phase. The empty areas of each brick row were filled with mortar. The finished rows and the material samples were cured after the end of each row. No frame was used for the door and window openings to allow free movement of the piers. Before building the roof, the foundation was filled with fresh grout to prevent lateral movement and separation between the specimen and the table. The roof beams and steel grid were installed, and the walls were drilled to add the roof-to-wall connection hooks. The wall-to-shotcrete connection hooks were installed before the roof concrete was cast.

Figure 6. URM specimen construction procedure

The rehabilitation of the damaged URM specimen was carried out after the URM tests were completed, in the order shown in Figure 7. At first, the collapsed parts of the specimen during the URM test were relocated. In follow, the vertical shotcrete rebars were spliced to the foundation rebars and roof hooks, and the horizontal rebars were then attached to the vertical rebars. The steel grid was connected to the walls by drilling through the thickness of the walls and installing the wall hooks. The northwest and the southeast holes were drilled, and the wall-to-wall connection hooks were added to each corner of the specimen. The walls were moisturized with water before applying the shotcrete layer, and the concrete and rebar samples were collected during the application of the shotcrete layer. The whole retrofitting procedure was carried out in one day. In the end, the additional mass blocks were placed on the roof, and steel cable with 12 mm diameter was used to fix the blocks to a series of closed hooks pre-installed in the center and corners of the roof concrete during the construction process.

Figure 7. Specimen rehabilitation procedure

The finished view of the URM and RM specimens before the tests is shown in Figure 8. Note that in Figure 8(II-b), the southwest corner of the RM specimen is viewed from inside. As shown in Fig (I), the interior face of north, and east walls, and the exterior faces of the south wall were covered by a thin plaster film to clarify the extent of the cracks.

(a) Northeast corner (b) Southwest corner (a) Northeast corner (b) Southwest corner

(I) Unretrofitted specimen (II) Retrofitted specimen

Figure 8. View of the (I) URM and (II) the RM specimen

Common to similar experimental studies [42], the care given to the specimen during construction was somewhat greater than in conventionally-built buildings: whereas the curing of typical masonry buildings is carried out after fabricating two or more brick rows considering the environmental humidity [43], the specimen of this study was watered once after each row. Therefore, the shear capacity of the mortar was increased [42] yet remained analogous to the shear strength in local buildings. The latter allowed more rocking motions in the piers and enabled the cracks to pass through the bricks. The frequent curing was because dry rows could have collapsed under the extra mass of the upper row, due to the use of the half-scale bricks. Hence, the extra watering ensured the integrity of the brickwork.

3.5 Instrumentation

A total of ten instruments consisting in eight accelerometers, and two Linear Variable Displacement Transducers (LVDTs) with were used to capture the acceleration and displacement in the key points of the specimen during both URM and RM tests. The layout of the sensors is shown in Figure 9, with the arrows indicating the positive direction of each sensor. The two LVDTs were attached to the middle of the south and west roof tie-beams to measure the roof displacement in each direction. For each direction, two accelerometers were installed at the roof elevation at the sides of the walls to capture the roof torsion as well as in-plane wall drifts, one accelerometer was attached to the northwest corner at the middle of the wall height to investigate the onset of rocking movement at the vicinity of the window opening, and another accelerometer was placed on the base at the southwest corner to derive the Fourier transfer functions and to measure the changes in the frequency content of the specimen response. In addition to the sensors, the motion of the specimen was recorded by high-resolution cameras with a 60 frames-per-second capture rate. After each step, the walls were inspected visually and by capturing high-definition photos to follow the extent of the cracks.

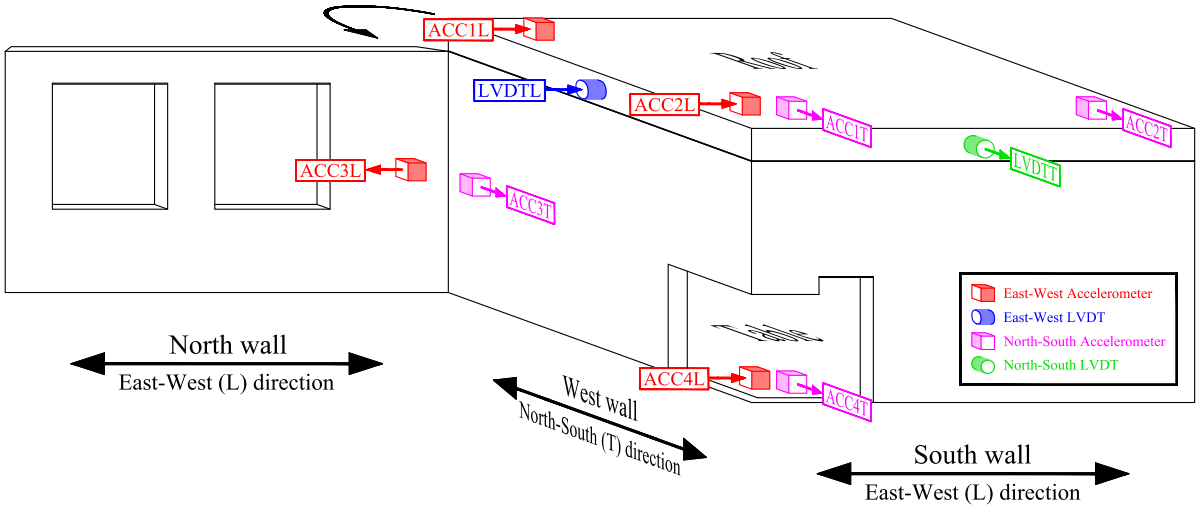

Figure 9. Arrangement of the sensors on the specimen

3.6 Input ground motion data

On February 22, 2005, an earthquake with a magnitude of 6.2 hit Zarand, Kerman, Iran. The event is considered as a shallow earthquake with 21 m epicenter depth. The damage and casualties of the earthquake were significant with the death toll of 612 and an estimated 1450 injuries [44]. Zarand ground motion was used in this study as input excitation

to represent a strong local earthquake. Due to shake table limitations, the vertical component of the earthquake was not used. The longitudinal and the transverse components were applied to the L and T directions of Figure 2(a), respectively. The peak ground acceleration (PGA) of each component was scaled to Tehran's response spectrum (0.35g) and then, Cauchy's acceleration and time scale factors were applied to the data; i.e., the acceleration values and the time steps were multiplied and divided by two, respectively. The time history and the pseudo acceleration response spectrum of the scaled components are shown in Figure 10.

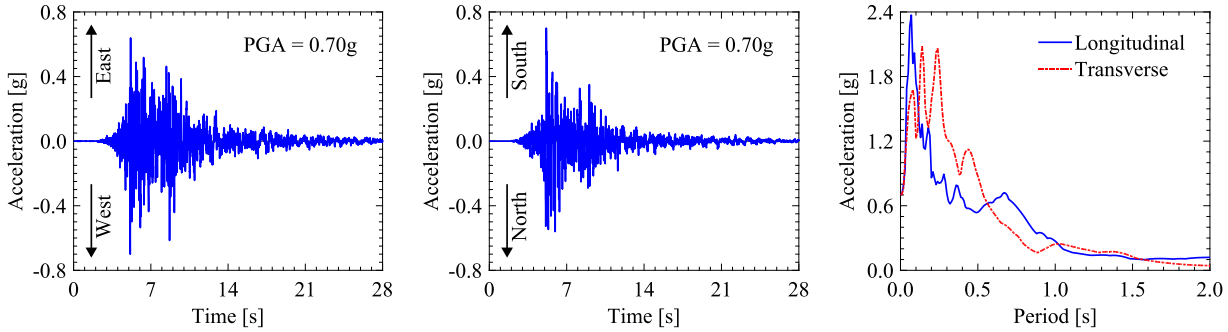

(a) Longitudinal accel. time-history (b) Transverse accel. time-history (c) Pseudo accel. response spectrums

Figure 10. Zarand ground motion adapted for the half-scale specimen

4. Shake table test results

The stepwise excitation information, including the shake table Peak Ground Displacements (PGDs) and Peak Ground Accelerations (PGAs), is presented in Table 3 for both URM and RM tests. Prior to the tests, a Finite Element (FE) model of the URM specimen was developed in the commercial software Abaqus, and the ground motion was applied to the model in different intensities. The results indicated the L direction walls, especially the north wall, as the weakest parts of the specimen with a rocking failure mode. Therefore, during all seven steps of the URM test, the intensity of the longitudinal excitation was held at 3/4 of the transverse excitation to prevent the in-plane collapse of north wall piers; both components were increased proportionally at each step.

Table 3. Excitation sequence of the shake table tests

Step	URM test				RM test			
	L direction		T direction		L direction		T direction	
	PGD [cm]	PGA [g]	PGD [cm]	PGA [g]	PGD [cm]	PGA [g]	PGD [cm]	PGA [g]
Step 1	0.40	0.07	0.38	0.09	3.56	0.64	3.50	0.85
Step 2	0.80	0.14	0.77	0.19	5.31	0.96	5.27	1.27
Step 3	1.60	0.29	1.55	0.37	7.05	1.27	6.97	1.69
Step 4	3.22	0.58	3.11	0.75	8.82	1.60	6.97	1.69
Step 5	4.83	0.87	4.67	1.13	10.60	1.92	6.97	1.69
Step 6	5.66	1.02	5.61	1.36	10.60	1.92	6.97	1.69
Step 7	6.83	1.24	6.73	1.63	8.82	1.60	6.97	1.69
Step 8	—	—	—	—	10.60	1.92	6.97	1.69
Step 9	—	—	—	—	10.60	1.92	6.97	1.69

The first step of the RM test was conducted with 50% of the PGAs used in the final step of the URM test. The PGAs were increased at the second and the third steps with the same 3/4 proportion. At the third step of the RM test, the shake table reached the ultimate excitation capacity in T direction and hence, from the fourth step forward, the PGA of the transverse excitation was kept constant. In the first three steps of the RM test, no significant damage was observed in the RM specimen; therefore, the longitudinal component of the fourth step was increased to the same PGA as of the transverse component. In the fifth step, the longitudinal excitation was 15% increased, and the sixth step was conducted with the same PGAs of the fifth step because the limit PGAs of the shake table were reached in both directions. At the seventh step, the connection between the foundation and the vertical rebars of the RM specimen was

released; therefore, the same PGAs of the fourth step were applied to the specimen to first investigate the magnitude of the rocking movement before imposing irreversible damage to the specimen. The eighth and ninth steps were again conducted with the same PGAs as of the sixth step, i.e. the ultimate excitation capacity of the shake table. Note that the information of Table 3 are directly recorded from the shake table and may exhibit minor differences with the intended PGAs and proportions.

4.1 Visual observations

After each step of the tests, the walls were inspected visually to identify propagated cracks. Some of the significant cracks, especially the ones caused by the rocking motions, were overlooked in the visual investigations during the test and were detected only by reviewing the videos. Figure 11 shows the crack pattern of the URM specimen alongside the photos of the major cracks. During the URM tests, the specimen showed almost no visible crack until Step 6, which corresponds to 1.02g and 1.36g PGAs in L and T directions, respectively. As the most remarkable observation, during the last step of the test, the middle pier in the north wall lost arching action and collapsed due to the rocking motion of the walls in T direction; however, the continuous lintel beam preserved the integrity of the specimen. Both the north and the south walls showed failure modes that were mainly caused by the interaction of in-plane and out-of-plane deformations. In the south wall, the in-plane deformation left a near-horizontal crack at the top corners of the door, and the rocking of the specimen in north-south direction caused a crack at the base of the wall. In the north wall, in addition to the combined in- and out-of-plane deformations, the eccentricity of the openings played a significant role in the propagation of crack and the failure mode of the solid perpendicular walls. In the left pier where the window opening was closer to the wall end, the rocking movement of the east wall was initiated almost at the elevation of the bottom left corner of the opening, which in return resulted in a near-horizontal crack at the bottom of the left pier. At the wider right pier, the in-plane crack at the bottom corner of the opening was declined to the base, and the damages of the rocking in the west wall were limited to a small crack at the bottom corner of the wall. Investigating the damages at the roof elevation showed that the roof-to-wall connection hooks, implanted in the thickness of the walls, prevented the sliding of the roof all across the walls. At the intersection of the perpendicular walls in the corners of the specimen, the brick configuration of the wall connections proved to serve well as no concentrated damage was observed at the wall connections.

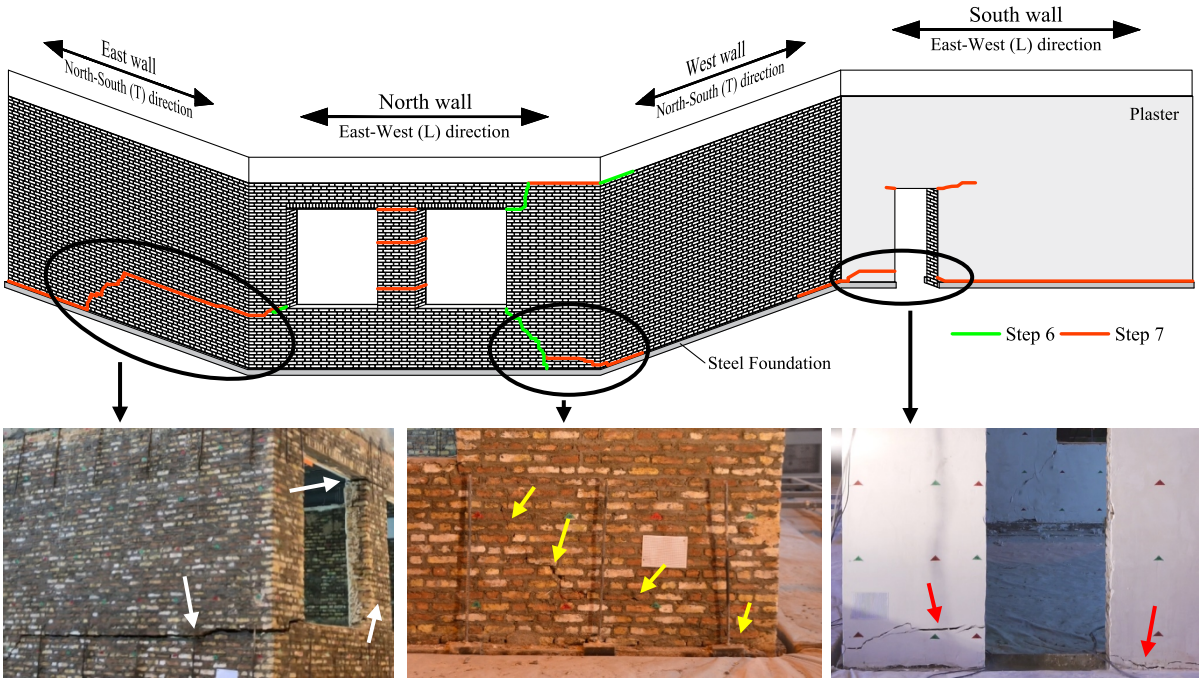

Figure 11. Crack propagation map of the exterior face of the URM specimen

In the RM specimen, each wall had two faces with different materials; thus, each side of the walls was separately investigated for propagated cracks. Figure 12 shows the crack propagation in the exterior and the interior face of the walls during the RM test. The first cracks were developed during Step 2, which was conducted with 0.96g and 1.27g PGAs for L and T components, respectively. The most important observation was that the cracks in the RM specimen were opened from the same locations they were previously developed in the URM specimen. At higher intensities in

the last steps, these cracks propagated more and pushed the specimen to the verge of collapse. For example, in the south wall, the in-plane cracks at the top right corner of the door reached the middle parts of the wall and inclined to the right corner; the crack at the top left corner of the door also propagated to the wall face and opened a horizontal crack in the west wall.

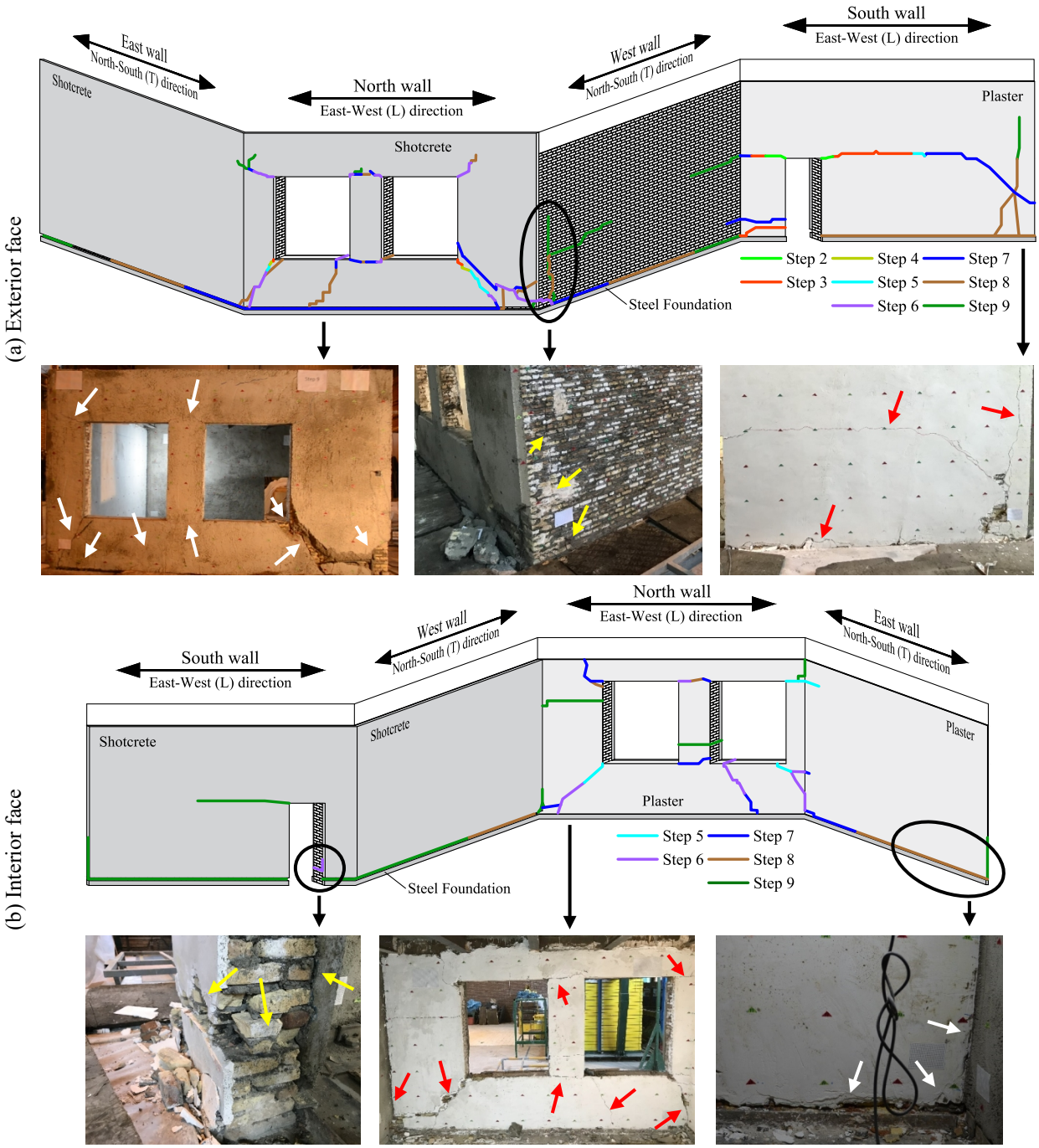

Figure 12. Crack propagation maps of the (a) interior and (b) exterior faces of the RM specimen

As shown in the crack propagation maps, the rocking movement of the east and the west walls was completely restrained due to the connection between the foundation and the shotcrete vertical rebars; the walls were exposed to rocking motion only during the last three steps of the RM test where the connections were released. Opening the connection also affected the behavior of the L direction walls. For instance, during Step 7, the cracks at the corners of the window opening in the north wall were strictly developed because of the rocking of the walls in T direction. The shotcrete and the retrofit details prevented further propagation of the damages that were already propagated during

the URM test. As an example, in the north wall, the shotcrete-to-wall connection hooks held the relocated middle pier in place and preserved the integrity of the wall during all steps. Moreover, the rocking crack that was previously developed in the mid-height of the east wall during the URM test remained closed throughout the RM test, and the rocking motion of the retrofitted wall caused a new horizontal crack at the base of the wall. However, in the right corner of the north wall, the shotcrete was not able to prevent the re-opening of the in-plane crack, and severe delamination was observed between the shotcrete and the brick layer. In regard to the shotcrete-to-roof connection, the hook between the shotcrete layer and the roof completely solidified the connection and prevented relative movement between the two parts. At the connection between the shotcretes of the perpendicular walls, two vertical cracks were opened on the masonry face of the south and west walls, next to the exterior-to-interior shotcrete connections of the southeast and northwest corners, respectively. In contrast, the exterior-to-exterior, and interior-to-interior connections of the shotcrete layers in the northeast and the southwest corners did not exhibit any damage. The shotcrete and the brick layer of the north wall demonstrated an intense composite action as all cracks developed on the exterior face had a counterpart on the interior face. However, in a few regions, the two layers acted as separate components: (1) At the left pier of the south wall, the out-of-plane crack at the bottom of the pier was re-opened and propagated to the interior face through the thickness of the brick layer; although, instead of aiding the masonry part, the shotcrete remained intact, and the crack was redirected in an upward direction, separating the two layers. (2) The exterior horizontal cracks in the mid-height of the west wall also did not have a reflection on the interior face.

4.2 Response in time domain

This section presents the results of processing the instrumentation outputs. As described, the shake table tests were carried out in a total of 16 steps, including seven URM and nine RM steps. Ten sensors were used to capture the displacements of the specimens in each step, which resulted in the collection and process of 160 signals in total. The accelerometer outputs were converted to displacement through double direct integration and were used as redundant displacement recorders, in addition to the LVDTs. An example for the accuracy of double integration is shown in Figure 13, in which for Step 5 of the RM test, the displacement derived from the roof accelerometers in L direction is averaged and compared to the roof LVDT outputs. For each direction, the displacement of the shake table was subtracted from the LVDT output to calculate the average drift of the roof. The torsion at roof elevation during each step was calculated by double-integrating the difference between the outputs of the roof corner accelerometers in each direction. Furthermore, the peak in-plane drift of each wall was separately derived by calculating the maximum relative displacement between the adjacent roof accelerometer and the shake table. Table 4 summarizes the average drift of the roof, the maximum drift captured at the roof corners, and the roof torsion at each step of the URM and RM tests. The maximum drift in L and T directions correspond to in-plane drift of the north and west walls, respectively.

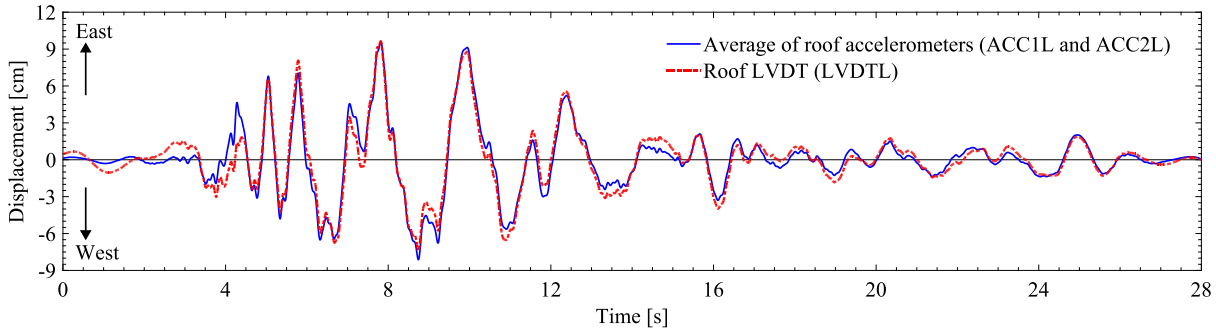

Figure 13. Comparison between the displacement from L dir. roof accelerometers and LVDT, Step 5 of the RM test

The results of Table 4 for the URM test are illustrated in Figure 14, where the average drift of the specimen is compared to the in-plane drift of the walls at various PGAs. The difference between wall drifts in each direction is caused by the roof torsion because of the stiffness eccentricity that is resulted from the openings of L direction walls. Clearly, the difference has raised in higher PGAs as the progressive damage of the walls increases the stiffness eccentricity. Before Step 4, all curves show an almost linear behavior as the specimen has not yet experienced any significant damage. The stiffness degradation of the URM specimen is initiated from Step 5, which corresponds to PGAs of 0.87g and 1.13g for L and T directions, respectively. As shown in Figure 11, no visible crack was sighted in Step 5. Hence, the minor stiffness change may refer to hidden cracks that became evident during Steps 6 and 7. In the last step of the URM test, all parameters have experienced a significant jump, which can be justified by the cracks observed at the bottom of the walls, indicated in Figure 11.

Table 4. Summary of drift ratios and torsions of the specimens

Step	URM test					RM test				
	Maximum drift [%]		Average drift [%]		Torsion [$\times 10^{-2}$ rad]	Maximum drift [%]		Average drift [%]		Torsion [$\times 10^{-2}$ rad]
	L dir.	T dir.	L dir.	T dir.		L dir.	T dir.	L dir.	T dir.	
Step 1	0.07	0.09	0.05	0.06	0.03	0.58	0.63	0.41	0.48	0.19
Step 2	0.13	0.15	0.09	0.11	0.06	0.91	0.98	0.68	0.78	0.25
Step 3	0.25	0.29	0.18	0.20	0.10	1.22	1.36	0.95	1.09	0.31
Step 4	0.55	0.63	0.40	0.47	0.20	1.61	1.77	1.29	1.43	0.41
Step 5	0.95	1.09	0.74	0.87	0.32	2.07	2.19	1.63	1.81	0.52
Step 6	1.31	1.47	1.02	1.19	0.41	2.15	2.31	1.69	1.91	0.55
Step 7	2.17	2.32	1.71	1.81	0.59	1.79	1.98	1.44	1.62	0.45
Step 8	—	—	—	—	—	2.44	2.65	1.85	2.05	0.60
Step 9	—	—	—	—	—	2.59	2.91	1.98	2.29	0.62

The response of the walls in the URM specimen is evaluated by comparing their in-plane drifts with the performance level acceptance criteria presented in Table 11-4 of ASCE 41, shown in Figure 14. In this figure, IO, LS, and CP correspond to Immediate Occupancy, Life Safety, and Collapse Prevention performance levels, respectively. Based on ASCE 41, at IO limit, the building does not experience any notable damage, and only a minor stiffness degradation occurs. At LS limit, the building undergoes severe damages that may be repairable. Finally, the building is on the verge of collapse in CP limit with severe residual deformations. As the crack propagation map in Figure 11 shows, all walls exhibited rocking failure mode. Accordingly, the ASCE 41 drift limits provided for single walls and piers subjected to rocking motion, which are directly related to the height-to-length ratio of the walls, were used. The LS and CP drift limits of the north and the south walls were considered as the minimum of the drift limits calculated for the piers of each wall; and since the piers of each wall had different geometry, different drift limits resulted from the provision. Comparing the damage curves and the crack observations with the drift limits highlights a disagreement between the behavior of the walls and the performance limits of ASCE 41; in all cases, the associated damage levels are achieved in larger drift ratios compared to the prediction of ASCE 41. For instance, in Figure 14(a), although the damage curve of the north wall shows no considerable stiffness degradation until Step 4, ASCE 41 conservatively holds Step 2 as the IO limit point. Furthermore, whereas the LS limit considers Step 3 as the beginning of significant damages in the north wall, both Figure 11 and Figure 14(a) confirm that the wall shows no considerable damage until Step 5. Similarly, where the CP limit suggests severe stiffness degradation and unrepairable damages in the north wall in Step 5, such observations are not made until Step 7. The same comparison goes to the south wall as well. For the walls in T direction, Figure 14(b) again confirms a contrast between the behavior of the walls and the anticipation of performance limits. ASCE 41 indicates that the west and the east walls surpass the CP limit during Steps 3 and 5, successively. Nevertheless, Figure 11 shows that no crack appears in these walls until Step 7. The interesting phenomenon at work is, in fact, the effect of perpendicular walls on the boundary condition of the T direction walls. Where the east and the west walls should have exhibited rocking motion in earlier steps, the undamaged north and south walls acted as constraints and postponed the major defection; the T direction walls were able to deform freely only after the in-plane cracks of the north wall were developed. In addition, the jump in the drift curves of L direction walls during Step 7 is also caused by the rocking motion of the T direction walls as the result of interaction between the two directions. A more surprising observation was that in Step 7, the east wall exhibited more severe damages than the west wall, despite its drift being the lowest of the two walls. This can also be justified by referring to the eccentricity of the openings in the north wall. According to Figure 11, during Step 6, the in-plane crack of the pier with smaller width in the north wall reached the corner of the specimen; in contrast, the cracks in the wider pier dissipated to the base of the wall. Consequent to the orientation of the cracks, the potential for rocking motion became higher in the east wall compared to the west wall. Note that, the performance limits provided in ASCE 41 are based on quasi-static tests on single piers and walls and are proven to give conservative results when applied to more complex cases such as the walls which intersect other walls. Similar observations were made in the experimental study of Yi et al. [45] on a two-story URM building, where the provision significantly underestimated the strength of the walls, and the failure modes of the walls were altered because of the interaction of perpendicular walls.

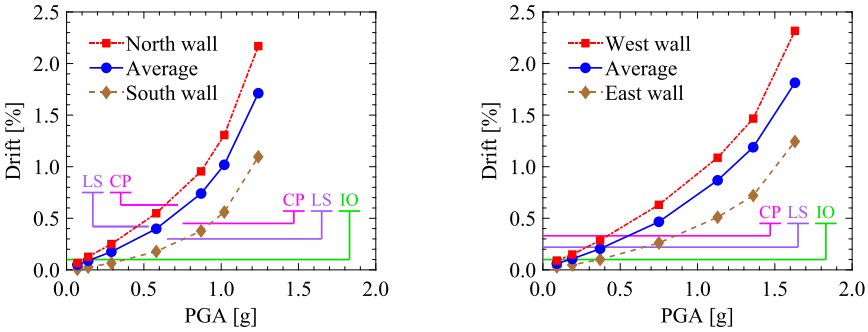

(a) L direction (b) T direction

Figure 14. Comparison between average story and wall drifts in the URM specimen

As previously mentioned, while the drift curves of Figure 14 show that the first significant stiffness decrease in the URM specimen has occurred in Step 5, no cracks were observed during this step. An investigation is made herein to verify previous observations and to identify the nature of the damages during Steps 5 and 6.

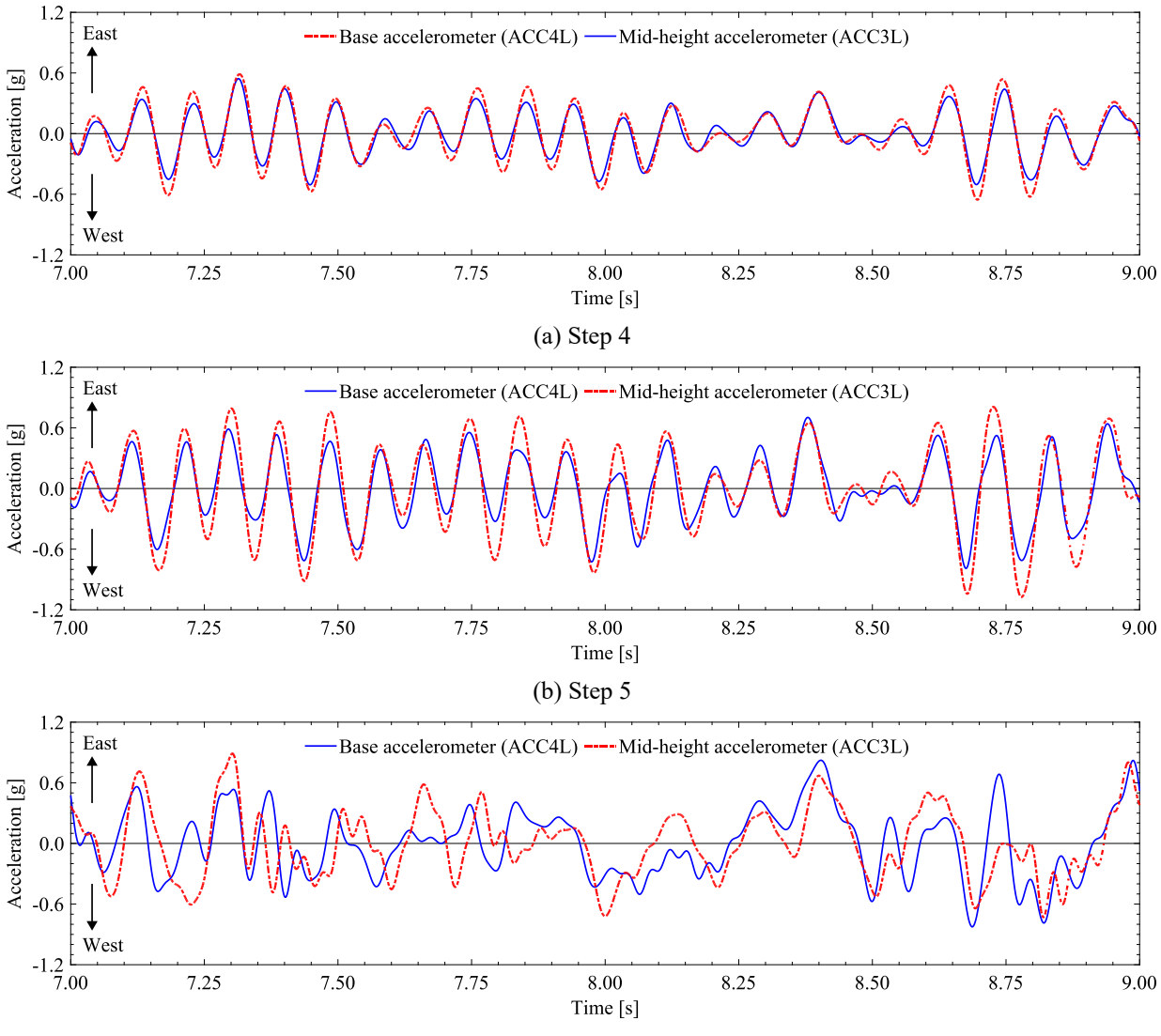

(a) Step 4

(b) Step 5

(c) Step 6

Figure 15. Response of the URM specimen at base and mid-height (northwest corner) elevations in L direction

Previous studies [42] consider the effects of rocking motion on the specimen, in terms of the time-history response, as a jump between the output of the sensors. Similarly, the beginning of softening and crack development is identified through detecting the phase shift between the response of the sensors. As depicted in Figure 11, the first cracks of the URM specimen were mainly developed at the corner of the wider opening in the north wall during Step 6. In addition, as observed in Figure 14, during Step 5, the north wall has shown the most considerable stiffness decrease amongst the walls of the specimen. Therefore, the output signals of the mid-height and base accelerometers in L direction during a two-second interval of Steps 4, 5, and 6, shown in Figure 15, are used to identify the onset of the rocking motion, and the step corresponding to the initiation of cracks. Comparing the sensor outputs during Steps 4 and 5, respectively shown in Figure 15(a) and Figure 15(b), shows that concurrent to the drift jump in Step 5, the response of the mid-height sensor has experienced a noticeable jump compared to the outputs of Step 4; although, no phase shift is observed between the response of the two sensors. Therefore, it can be concluded that the rocking motion of the north wall is started in Step 5, without causing any deteriorating damage to the wall. In Step 6, at the same time that the first cracks appear in the corners of the north wall openings, a significant distortion and an evident phase shift occur between the response of the two sensors, as shown in Figure 15(c). Clearly, the severe changes confirm Step 6 as the beginning of crack propagation and softening of the specimen.

The average drifts and roof torsion of the URM and RM specimens are compared in Figure 16. The results show that the shotcrete layer has been able to postpone the stiffness degradation to a much higher level of excitation in Step 5 of the RM test. The initial tangent of the RM specimen drift curves in Figure 16(a) and Figure 16(b) are almost equal to the drift slopes in the first three steps of the URM curves. This means that the shotcrete layer has been able to compensate for the damages of the specimen and generate the same stiffnesses as of an undamaged URM specimen. More interestingly, Figure 16(c) shows that compared to the URM test, the shotcrete layer has improved the overall integrity of the RM specimen and has decreased the torsion slope in all steps except the last three. In Step 3 of the RM test which almost had the same PGAs as of Step 7 in the URM test, the RM specimen showed 44, 40 and 47% decrease in the average longitudinal drift, average transverse drift, and roof torsion, respectively, while maintaining a linear behavior. The longitudinal drift curve of the RM specimen also shows almost 55% strength increase compared to the URM curve at 1.70% drift. The effects of interaction between the walls of the two directions can be found in the transverse drift curve of the RM specimen, Figure 16(b), where despite the constant excitation intensity from Steps 3 to 6, the drift values have raised because of the increasing excitation of L direction. As mentioned, in the last three steps of the RM test, the vertical rebars were released from the foundation, and the RM specimen was exposed to rocking movement. The corresponding drift data are shown in Figure 16 with red cross marks. The release of the connection between the foundation and vertical rebars caused a noticeable decrease in the stiffness of the RM specimen in both directions, from Step 7 forward. Likewise, as depicted in Figure 12, the rocking cracks were only observed during and after the seventh step. Another indication of the interaction between the perpendicular walls is made in Figure 16(a) where during Step 7, the stiffness of the RM specimen in L direction is also decreased as the result of the damages in the north wall that were caused by the rocking motion of the walls in T direction.

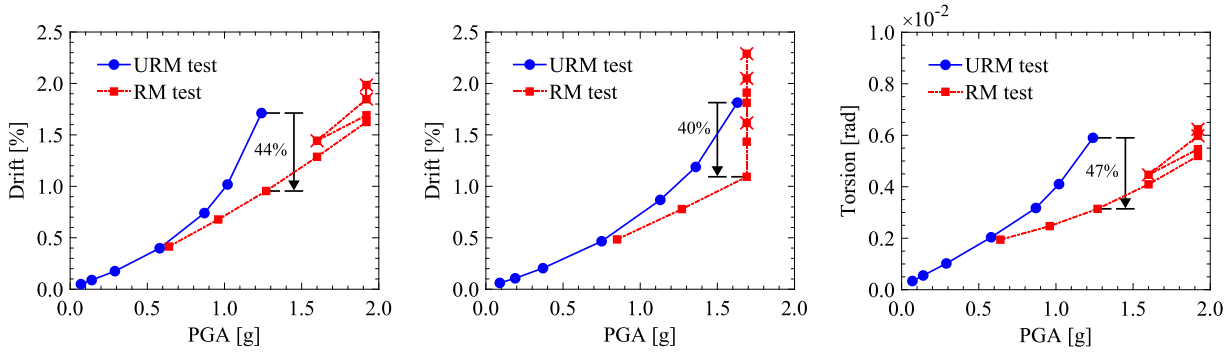

(a) Average longitudinal drifts (b) Average transverse drifts (c) Roof torsion

Figure 16. Comparison between the average dirfts and torsions of the URM and RM specimen

4.3 Frequency domain observations

The outputs of the accelerometers in each step of the tests were used to determine the dynamic properties of the specimen. Preliminary modal analysis of the undamaged URM specimen showed five principal and nine local vibration modes within the range of 0-20 Hz frequencies. Of the five primary modes, that are illustrated in the appendix, the first and the second modes contributed to the translation of the structure in L and T directions,

respectively. The third mode was related to the vertical translation of the roof, and the fourth mode represented local out-of-plane deformation of the middle pier in the north wall. Finally, torsion of the building participated in the fifth mode. Further simulations showed the same vibration modes for the RM specimen as well. In the transient segment of the excitations where the specimens had an almost free-vibration motion, the Fast Fourier Transform (FFT) of the average response of the roof accelerometers in each direction was normalized to the FFT of the base accelerometer output in order to find the frequencies of the first and the second modes. In addition, the FFT of the response of each roof accelerometer was normalized to the corresponding FFT of the base accelerometer, and in each direction, the transfer functions resulted for each roof corner were compared to find the torsional frequency of the roof. By assuming the mass participation of the specimens in each mode to remain intact throughout the test steps, the changes in the frequencies can be directly related to the stiffness degradation of the specimen, which in return indicates the severity of the cumulative damages the specimen has taken until the end of each step. Therefore, similar to the works of Mendes et al. [28], a damage index is defined, as in the following, to quantify the damages related to each vibration mode.

$$DI_n = 1 - f_n / f_1 \tag{1}$$

For each deformation mode, DI_n is the damage index for cumulative stiffness degradation until the end of the n^{th} step, f_n represents the frequency of the specimen after the n^{th} step, and f_1 is the frequency of the specimen at the first step. The frequencies and the damage indices of the translational and the torsion modes are summarized in Table 5. Note that torsion is presented as the third vibration mode because of the insignificant contribution of the other modes.

Table 5. Frequencies and damage indicators of URM and RM tests (all values are in Hz)

Step	URM test			RM test		
	1st mode (L translation)	2nd mode (T translation)	3rd mode (Roof torsion)	1st mode (L translation)	2nd mode (T translation)	3rd mode (Roof torsion)
Step 1	11.13 (0.00)[1]	12.73 (0.00)	14.15 (0.00)	8.77 (0.00)	9.60 (0.00)	11.09 (0.00)
Step 2	11.13 (0.00)	12.73 (0.00)	14.11 (0.00)	8.67 (0.01)	9.52 (0.01)	11.09 (0.00)
Step 3	10.99 (0.01)	12.51 (0.02)	13.75 (0.03)	8.32 (0.05)	9.12 (0.05)	10.20 (0.08)
Step 4	10.47 (0.06)	12.00 (0.06)	13.27 (0.06)	8.21 (0.06)	8.92 (0.07)	9.87 (0.11)
Step 5	8.52 (0.23)	10.55 (0.17)	12.33 (0.13)	7.71 (0.12)	8.73 (0.09)	8.62 (0.22)
Step 6	6.60 (0.41)	8.76 (0.31)	10.65 (0.25)	7.27 (0.17)	8.03 (0.16)	8.23 (0.26)
Step 7	5.16 (0.54)	6.69 (0.47)	9.02 (0.36)	6.36 (0.27)	7.12 (0.26)	7.65 (0.31)
Step 8	—	—	—	5.14 (0.41)	6.64 (0.31)	6.51 (0.41)
Step 9	—	—	—	4.36 (0.50)	5.87 (0.39)	6.30 (0.43)

[1]The values in the parenthesis represent the damage index of the corresponding frequency.

Amongst the results of Table 5, the RM specimen contains much lower frequencies, compared to the URM specimen. As previously mentioned, a 64 kN artificial mass was added to the roof before the RM test. Furthermore, the addition of the shotcrete layer increased the total mass of the RM specimen by 33.2 kN. A simple investigation is made herein to determine to what extent the extra masses contribute to the frequency decrease. According to the fundamental relation between stiffness, mass, and natural frequency of a single degree of freedom system, stiffness is in direct relation to the mass times the second power of frequency. As discussed, Figure 14 shows that for translation in each of L and T directions, the initial stiffness of the specimens are seemingly equal. Consequently, the proportion between the initial frequencies of the specimens in each vibration mode can be inversely related to the square root of the proportion between the participating mass of the specimens in that vibration mode. The cracks of Figure 11 and Figure 12 lead to the deduction that in both specimens, all regions except the bottom spandrel of the north wall participate in the translation in T direction; i.e., 88% of the total mass of the walls participates in the second mode. By considering the full contribution of the additional roof mass and neglecting the slippage between the mass blocks and the roof, 12.24 and 21.56 ton will be respectively calculated as the total participating mass of the URM and RM specimens in the second vibration mode. These values result in 0.753 as the proportion between the initial frequencies of T translation mode, which is equal to the proportion between the 12.73 and 9.60 Hz frequencies, and interestingly implies that the decrease in the frequency of the RM specimen is exclusively caused by adding the artificial roof mass and the retrofit layer.

Figure 17 compares the damage indices of each vibration mode for the URM and RM specimens. In all curves, slight damages are observed in the first four steps, which were not visible in the drift curves of Figure 16. However, the magnitude of the initial damages is within 10-13% of the final damages, satisfying the LS performance limit. In all figures, the first significant damage of the URM specimen occurs in Step 5, which confirms the previous observations in Figure 14. The first effects of the retrofit layer can be observed in Step 3 of the RM test where despite the PGAs are almost equal to the last step of URM test, the damages of the L translation, T translation, and roof torsion in RM specimen are respectively 95, 89, and 78% lower than those of the URM specimen. During Steps 5 and 6 of the RM test, the L translation damage curve shows more serious cumulative and stepwise damages compared to the T translation curve; again, implying that the L translation mode is the dominant mode of deformation. Surprisingly, during Step 7, releasing the connection between the vertical rebars and the foundation affected the L translation mode more than the T translation mode; this observation also refers to the interaction between the walls in two directions. Before opening the foundation connection, the damages in T direction were mainly concentrated at the base of the walls. When the connection was released, the base of the east and the west walls were already damaged. Consequently, the walls in L direction remained as the only components restraining the rocking motion of the specimen. During Step 7, the effects of T translation mode focused on the north and the south walls to break the constraint. As a result, the north wall which had a higher potential for out-of-plane defection took most of the damages and raised the overall damage in L direction. Although, this process was not limited to one step and lasted throughout Steps 7 to 9. Comparing the T translation damage curves of the URM and RM specimens in Figure 17(b), and the cracks of T direction walls in the specimen shows that the retrofit layer has lowered the total damage of the T direction walls by preventing the URM cracks from re-opening, and redirecting the stress to the milder cracks at the base of the walls. Figure 17(c) also shows that the torsional damage of the RM specimen is higher than the URM specimen.

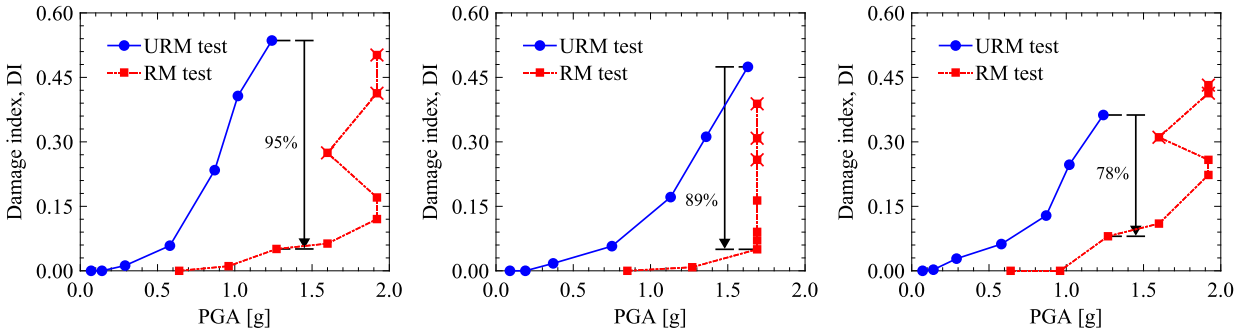

(a) Longitudinal average drifts (b) Transverse average drifts (c) Roof torsion

Figure 17. Comparison between the damage curves of the RM and URM specimen

The spacing of the shotcrete and connection rebars was 3-5 times the spacing used by DRES [32], as there was no guarantee that the limited intensity of the shake table could damage a specimen with smaller spacings. Consequently, as shown in Figure 17, the RM specimen showed culminated damages in each deformation mode, because the masonry part and the concrete took most of the damage. Moreover, the delamination in the northwest and southwest corners of the RM specimen, illustrated in Figure 12, may have been caused by the large reinforcement spacings. The excellent durability of the specimen in high PGAs, however, ensured that a prototype with typical 10-15 cm rebar spacings [32] can undergo even stronger earthquakes.

5. Conclusion

This paper presents the results of a series of shake table tests on a masonry building, unreinforced and retrofitted. The specimen was a half-scale model of a commonly built Iranian classroom with dimensions of 7.4×7.4×4.0 m. Similar to the classrooms, the specimen included two solid walls in one direction and for the other direction one wall with a door opening and the other with two eccentric window openings. In the first phase of the test, the unreinforced specimen was subjected to seven steps of increasing bidirectional shake table test. The test proceeded until severe cracks were observed on the walls. Subsequently, the damaged specimen was rehabilitated with shotcrete, two walls from the exterior face and the other two from the interior, and the second phase of the test was carried out in nine increasing intensity steps. At each step of the tests, the walls were accurately visually inspected to detect the developed cracks. The deformation of the specimen in terms of wall drift and roof torsion was captured in each step by employing high precision instrumentation. The objective of the test was to investigate the performance of the unreinforced specimen and the effects of rehabilitation on the already damaged model. Moreover, the specially designed details of wall-to-wall and roof-to-wall connections of the retrofitted specimen were evaluated during the tests. The effects of

restraining the shotcrete vertical rebars into the foundation were also investigated by closing and releasing the proposed rebar-foundation connection in various steps. Based on the results, it can be concluded that:

- No concentrated damage was observed at the intersection of perpendicular walls in the URM specimen. This proves that the proposed brick configuration for the wall connections has provided satisfactory integrity between the intersecting walls.
- Interaction of perpendicular walls has highly influenced the crack pattern and behavior of the walls. This effect has generally increased the capacity of the walls. Also, the deformation capacity of the walls was larger than predicted by ASCE 41 as a result of the effect of intersecting walls. For instance, in the case of rocking motion, the perpendicular walls should be lifted to allow a wall to rock. This effect has not yet been thoroughly investigated in the codes.
- The rehabilitation method enhanced the overall strength and integrity of the specimen. The shotcrete layers covered the previously damaged areas and postponed the collapse of the specimen to higher excitation levels.
- In most regions of the specimen, the rehabilitation method created a strong bond between the shotcrete and the brick layer. In some areas, however, noticeable delamination was observed between the layers, which requires developing more comprehensive detailing.
- Of the three proposed connections for the shotcrete of the perpendicular walls, the exterior-to-exterior and interior-to-interior connections performed without concentrated damages. In contrast, severe cracks were developed at exterior-to-interior connections, namely a vertical crack at the intersection of the walls, extended to the mid-height of the wall.
- The fixity of shotcrete vertical rebars to the foundation played a crucial part in the deformation of the specimen. the rocking motion and out-of-plane deformation of the walls only appeared after opening the connection.

In the end, the results of this paper proved that the proposed rehabilitation strategy and connection details highly increases the performance of already damaged buildings. In other words, instead of demolishing and reconstructing new buildings, the damaged unreinforced buildings can be reliably rehabilitated. Though, more investigation is needed to select the proper rehabilitation approach and detailing based on the damage level the building has experienced.

Acknowledgment

The authors acknowledge the financial support provided by Ecole Polytechniquie Fédérale de Lausanne (EPFL) and Sharif University of Technology (SUT). Appreciation is also extended to Dr. Ali Bakhshi for running the shake table tests and Mr. Rajabigol for operating the data acquisition system. Lastly, special thanks go to Ostad Mahmoud Nasirifar, RIP, for constructing the specimen and helping with technical aspects.

Reference

1. Kuwata Y, Takada S, Bastami M. Bulding damage and human casualties during the Bam-Iran earthquake. *Asian Journal of Civil Engineering (Building and Housing)* 2005; **6**(1–2): 1–19.
2. Mahdizadeh A. *Report on retrofit procedure of school buildings in I.R. Iran*. Tehran, Iran: 2011.
3. Abrams D, S. Moghadam A, Bozorgnia Y, Yekrangnia M. Seismic retrofit of school buildings in Iran. *12th North American Masonry Conference*, Denver, Colorado, USA: 2015.
4. Juhásová E, Sofronie R, Bairrão R. Stone masonry in historical buildings — Ways to increase their resistance and durability. *Engineering Structures* 2008; **30**(8): 2194–2205.
5. Meguro K, Mayorca P, Guragain R, Sathiparan N, Nasrollahzadeh K. Shaking table experiment of masonry buildings and effectiveness of PP-band retrofitting technique. *Seisan Kenkyu* 2005; **57**(6): 534–537.
6. Blondet M, Torrealva D, Vargas J, Tarque N, Velásquez J. Seismic reinforcement of adobe houses using external polymer mesh. *Proceedings of 1st European Conference on Earthquake Engineering and Seismology*, Geneva, Switzerland: 2006.
7. Raman SN, Ngo T, Mendis P. A review on the use of polymeric coatings for retrofitting of structural elements against blast effects. *Electronic Journal of Structural Engineering* 2011; **11**: 69–80.
8. Mayorca P, Meguro K. Formulation of a simple method to design PP-band mesh retrofitting for adobe/masonry houses. *Bulletin of Earthquake Resistant Structure* 2009; **42**: 121–130.
9. San Bartolome A, Quiun D, Zegarra L. Effective system for seismic reinforcement of adobe. *The 13th World Conference on Earthquake Engineering (13WCEE)*, 2004.

10. Yamin LE, Phillips CA, Reyes JC, Ruiz DM. Seismic behavior and rehabilitation alternatives for adobe and rammed earth buildings. *The 13th World Conference on Earthquake Engineering (13WCEE)*, Vancouver, Canada: 2004.

11. Turer A, Korkmaz SZ, Korkmaz HH. Performance improvement studies of masonry houses using elastic post-tensioning straps. *Earthquake Engineering & Structural Dynamics* 2007; **36**(5): 683–705.

12. Nikooravesh M, Soltani M. Behavior of unreinforced masonry piers strengthened using centercore method; experimental investigation. *Construction and Building Materials* 2018; **189**: 236–244.

13. Dowling D, Samali B. Low-cost and low-tech reinforcement systems for improved earthquake resistance of mud brick buildings. *Proceedings of the Getty Seismic Adobe Project 2006 Colloquium*, Lahore, Pakistan: 2006.

14. Abrams D, Lynch J. Flexural behavior of retrofitted masonry piers. *KEERC-MAE Joint Seminar on Risk Mitigation for Regions of Moderate Seismicity*, Illinois, USA: 2001.

15. Abrams D, Smith T, Lynch J, Franklin S. Effectiveness of rehabilitation on seismic behavior of masonry piers. *Journal of Structural Engineering* 2007; **133**(1): 32–43.

16. Lin YW, Wotherspoon L, Scott A, Ingham JM. In-plane strengthening of clay brick unreinforced masonry wallettes using ECC shotcrete. *Engineering Structures* 2014; **66**: 57–65.

17. ElGawady M, Lestuzzi P, Badoux M. Retrofitting of masonry walls using shotcrete. *2006 New Zealand Society of Earthquake Engineering (2006 NZSEE) Conference*, 2006.

18. Shabdin M, Attari NKA, Zargaran M. Experimental study on seismic behavior of Un-Reinforced Masonry (URM) brick walls strengthened with shotcrete. *Bulletin of Earthquake Engineering* 2018; **16**(9): 3931–3956.

19. Ghiassi B, Soltani M, Tasnimi AA. Seismic evaluation of masonry structures strengthened with reinforced concrete layers. *Journal of Structural Engineering* 2012; **138**(6): 729–743.

20. *FEMA 356: Prestandard and commentary for the seismic rehabilitation of buildings*. Washington, D.C.: American Society of Civil Engineers for the Federal Emergency Management Agency (FEMA); 2000.

21. *ASCE 41: Seismic evaluation and retrofit of existing buildings*. Reston, VA: American Society of Civil Engineers (ASCE); 2017.

22. *A preliminary report on school buildings performance during M 7.3 Ezgeleh, Iran; earthquake of November 12, 2017*. Tehran, Iran: The Organization for Development, Renovation and Equipping Schools of Iran (DRES), and Earthquake Engineering Research Institute (EERI); 2017.

23. Yekrangnia M. *Inspection of Kermanshah earthquake*. Tehran, Iran: The Organization for Development Renovation and Equipping Schools of Iran (DRES); 2018.

24. Avila L, Vasconcelos G, Lourenço PB. Experimental seismic performance assessment of asymmetric masonry buildings. *Engineering Structures* 2018; **155**(December 2016): 298–314.

25. Carvalho EC. Seismic testing of structures. *11th European Conference on Earthquake*, Paris, France: 1998.

26. Mendes N, Lourenço PB. Seismic assessment of masonry "Gaioleiro" buildings in Lisbon, Portugal. *Journal of Earthquake Engineering* 2009; **14**(1): 80–101.

27. Tomaževič M, Klemenc I, Weiss P. Seismic upgrading of old masonry buildings by seismic isolation and CFRP laminates: a shaking-table study of reduced scale models. *Bulletin of Earthquake Engineering* 2009; **7**(1): 293–321.

28. Mendes N, Lourenço PB, Campos-Costa A. Shaking table testing of an existing masonry building: assessment and improvement of the seismic performance. *Earthquake Engineering & Structural Dynamics* 2014; **43**(2): 247–266.

29. *Criterion No. 697: Regulations for design of educational buildings*. Tehran, Iran: The Organization for Development Renovation and Equipping Schools of Iran (DRES); 2016.

30. Martha Schneider-Bürger. *Stahlbau-Profile*. Germany: Beratungsstelle f. Stahlverwendung; 1935.

31. *Subject 8: Design and construction of masonry buildings*. Tehran, Iran: Office of National Building Regulations; 2019.

32. *Technical retrofitting specifications and typical shotcrete details for masonry school buildings*. Tehran, Iran: The Organization for Development Renovation and Equipping Schools of Iran (DRES); 2011.

33. ACI Committee 318. *Building code requirements for structural concrete (ACI 318M-14) and commentary (ACI 318RM-14)*. American Concrete Institute (ACI); 2014.

34. *Publication No. 376: Regulations for seismic retrofiting of existing unreinforced masonry buildings*. Tehran, Iran: Planning and Budget Organization; 2007.

35. *ASTM A370: Standard test methods and definitions for mechanical testing of steel products*. vol. 155. American Society for Testing and Materials (ASTM); 2004.

36. *ASTM C109/C109M: Standard test method for compressive strength of hydraulic cement mortars*. vol. i. American Society for Testing and Materials (ASTM); 2008.

37. Atkinson RH, Amadei BP, Saeb S, Sture S. Response of masonry bed joints in direct shear. *Journal of Structural Engineering* 1989; **115**(9): 2276–2296.

38. *BS EN 1015-10: Methods of test for mortar for masonry*. London: British Standards Institution (BSI); 1999.

39. *ASTM C1314: Standard test method for compressive strength of masonry prisms*. American Society for Testing and Materials (ASTM); 2016.

40. *BS EN 772-1: Methods of test for masonry units*. London: British Standards Institution (BSI); 2011.

41. *ASTM C39: Standard test method for compressive strength of cylindrical concrete specimens*. American Society for Testing and Materials (ASTM); 2015.

42. Bothara JK, Dhakal RP, Mander JB. Seismic performance of an unreinforced masonry building: An experimental investigation. *Earthquake Engineering & Structural Dynamics* 2009; **41**(11).

43. *Publication No. 55: Technical specifications for construction works*. Tehran, Iran: Planning and Budget Organization; 2004.

44. United Nations Field Assessment Team. *Report on Zarand Earthquake*. 2005.

45. Yi T, Moon FL, Leon RT, Kahn LF. Lateral load tests on a two-story unreinforced masonry building. *Journal of Structural Engineering* 2006; **132**(5): 643–652.

46. Lourenço PB. Computational strategies for masonry structures. Delft University of Technology, 1996.

47. Oliveira D V, Lourenço PB, Roca P. Cyclic behaviour of stone and brick masonry under uniaxial compressive loading. *Materials and Structures (2006)* 2006(39): 247–257.

48. Aref AJ, Dolatshahi KM. A three-dimensional cyclic meso-scale numerical procedure for simulation of unreinforced masonry structures. *Computers and Structures* 2013; **120**: 9–23.

49. Wilding BV, Dolatshahi KM, Beyer K. Influence of load history on the force-displacement response of in-plane loaded unreinforced masonry walls. *Engineering Structures* 2017; **152**: 671–682.

Appendix A: Illustration of the primary deformation mode shapes

The presented study used the Finite Element modeling software Abaqus and two separate numerical models for simulations. First, a 3D micro-model based on the works of Lourenço [46] and Oliveira et al. [47], developed by Aref and Dolatshahi [48] and elaborately discussed in the studies of Wilding et al. [49], was employed to capture the exact pushover and cyclic response, failure modes, and crack patterns of the URM and RM specimens. Afterward, a simplified 3D meso-scale model was developed for seismic and modal analysis of the specimens, and was adjusted to give the same responses as the micro-scale models. Figure A1(i) shows a view of the meso-scale URM model in which each wall is considered as a partitioned single solid (C3D8R) element, with the elastic region of the behavior following the original mechanical properties of masonry units (E_m and ν_m). Visual illustrations of the five deformation modes discussed in the article are presented in Figures A1(ii) to A1(v) in the following order: displacement of the roof along L and T directions, torsion of the roof, vertical translation of the roof, and local buckling of the pier in the north wall. Only the frequencies corresponding to the first three presented mode shapes were discussed because adequate instruments were not available to capture and locally study the two other modes.

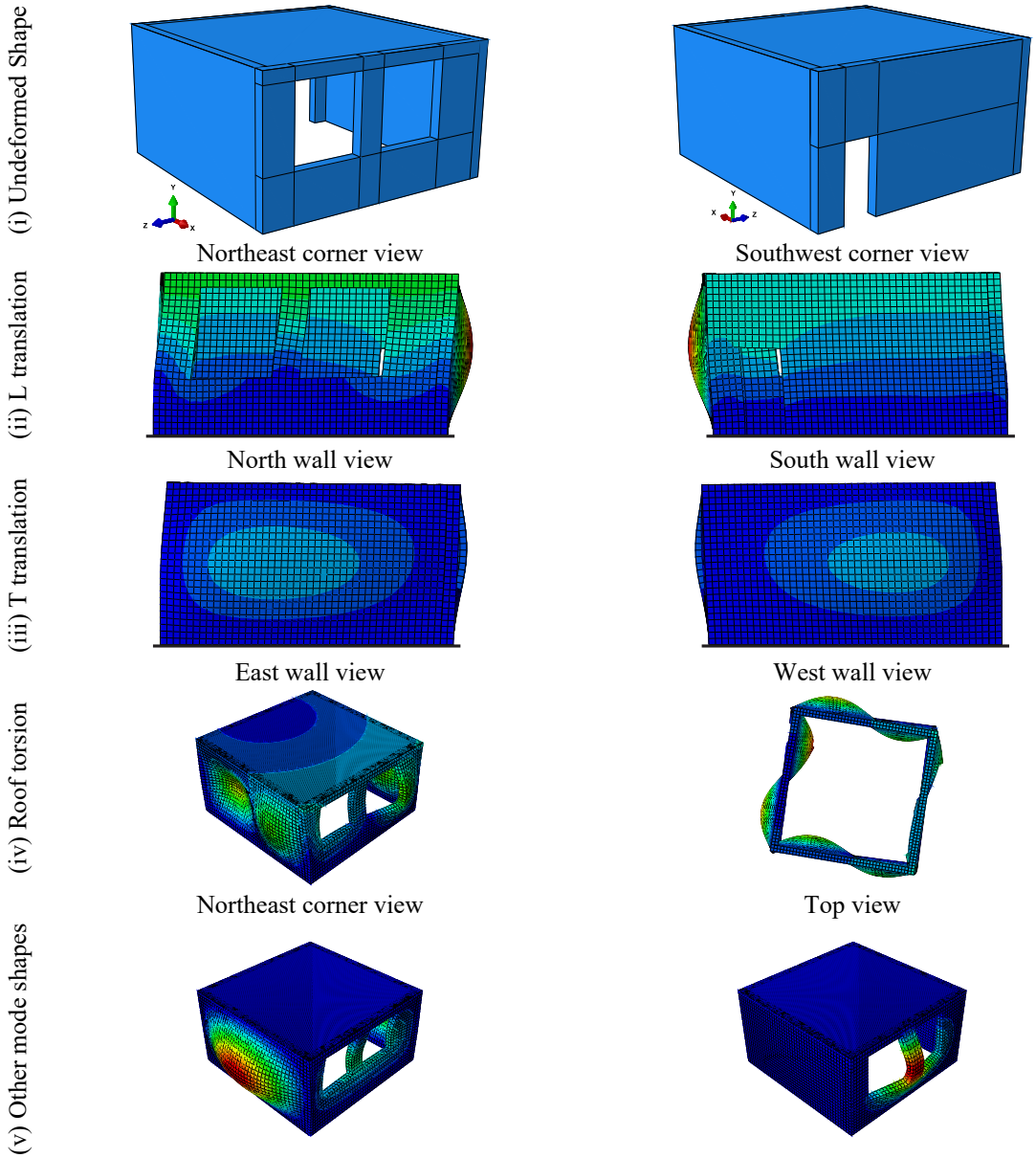

Figure A1. Undeformed view and mode shapes of the URM meso-scale FE model